electronic reprint

Journal of
Applied Crystallography
ISSN 0021-8898
Editor: **Gernot Kostorz**

Advances in digital topography for characterizing imperfections in protein crystals

Jeffrey J. Lovelace, Cameron R. Murphy, Henry D. Bellamy, Keith Brister, Reinhard Pahl and Gloria E. O. Borgstahl

Journal of
Applied Crystallography
ISSN 0021-8898

Received 22 October 2004
Accepted 22 March 2005

Advances in digital topography for characterizing imperfections in protein crystals

Jeffrey J. Lovelace,[a] Cameron R. Murphy,[a] Henry D. Bellamy,[b] Keith Brister,[c] Reinhard Pahl[c] and Gloria E. O. Borgstahl[a]*

[a]Eppley Institute for Research in Cancer and Allied Diseases, 987696 Nebraska Medical Center, Omaha, NE 68198-7696, USA, [b]CAMD/LSU, 6980 Jefferson Hwy, Baton Rouge, LA 70806, USA, and [c]BioCARS – The University of Chicago, 9700 South Cass Ave, Bldg 434B, Argonne, IL 60439, USA. Correspondence e-mail: gborgstahl@unmc.edu

A system which joins digital topography with fine φ-sliced reflection profiling has been developed and applied to cryocrystallography. In this demonstration, fifteen fine φ-sliced reflection profiles with corresponding topographic sequences are evaluated: twelve reflections from a crystal at cryogenic temperatures and three reflections from a room-temperature crystal. The digitally collected data show results comparable with film, albeit at a lower resolution, but are acquired at a substantially higher rate. Additionally, anti-blooming circuitry in the CCD was tested and shown to provide useful data even when pixels were overloaded.

1. Introduction

High-flux synchrotron radiation damages protein crystals. To prolong the useful life of samples for protein crystallography, the samples are typically cryocooled (cryo) during data collection. Although cryo conditions greatly increase the life span of the crystal, they can also have detrimental effects on the crystal. Cryo-induced changes that prevent optimal data collection can include large increases in the rocking width of the reflection, deformation and/or splitting of the reflection. To a first approximation, protein crystals are a mosaic of essentially perfect crystal domains, which are slightly misaligned with respect to one another (Darwin, 1922; Helliwell, 1988). Since the domains are slightly misaligned, they enter diffraction conditions at slightly different angles, leading to complex observed reflection profiles that are a composite of those from the individual mosaic domains (Fourme *et al.*, 1995; Nave, 1998; Boggon *et al.*, 2000; Vahedi-Faridi *et al.*, 2003). A greater domain misalignment causes the reflections to be spread out into larger spherical caps, resulting in broadened reflection profiles. Variation in the unit-cell dimensions could occur within a domain or between domains. These will result in a broadening of the reflection in the direction of the unit-cell variation. It is difficult to distinguish these two effects from the analysis of reflection profiles and mosaicity alone (Vahedi-Faridi *et al.*, 2003). What is needed is a complementary technique that can directly image the mosaic domains to help study these phenomena. Topography is one such approach.

Topography is the high-spatial-resolution imaging of an individual reflection. Typically, topographic measurements are done with nuclear emulsions or other high-resolution film (Fourme *et al.*, 1995; Stojanoff & Siddons, 1996; Stojanoff *et al.*, 1997, 1996; Dobrianov *et al.*, 1998; Otálora *et al.*, 1999; Boggon *et al.*, 2000). Film methods have many drawbacks that can be overcome by using a CCD detector with a small pixel size (~8 µm) (Ludwig *et al.*, 2001; Lovelace *et al.*, 2004; Lubbert *et al.*, 2004). Such high-resolution CCDs generally cover only a very small active area as compared with CCD-based area detectors commonly used in protein crystallography. The standard CCD detectors unfortunately have pixel sizes that are too large to be of use for topography. To overcome this issue, we use a large area detector to identify target reflections and then mechanically position the topography CCD based on this information. The approach is different from the one used by Lovelace *et al.* (2004). This novel method allows the detector to be quickly and parasitically installed at many existing beamlines, as shown in Fig. 1. As part of the testing process, several topographs and fine φ-sliced reflection profiles were collected from a lysozyme crystal under cryo and room temperature (RT) conditions. For topographic and fine φ-sliced data collection the beamline optics must be adjusted to provide a monochromatic and parallel beam.

2. Experimental methods

2.1. Crystal preparation

Cryo diffraction data for tetragonal lysozyme crystals have been successfully measured from samples soaked in 40% glycerol (Sauter *et al.*, 2001) or coated with oil (Kriminski *et al.*, 2002). In this study, these two methods were combined as follows. The crystals were mounted in a cryoloop (Hampton Research) after first being soaked for a few seconds in reservoir solution supplemented with 40% *v*/*v* glycerol; then dragged through an immersion oil mixture (type-A:type-NVH

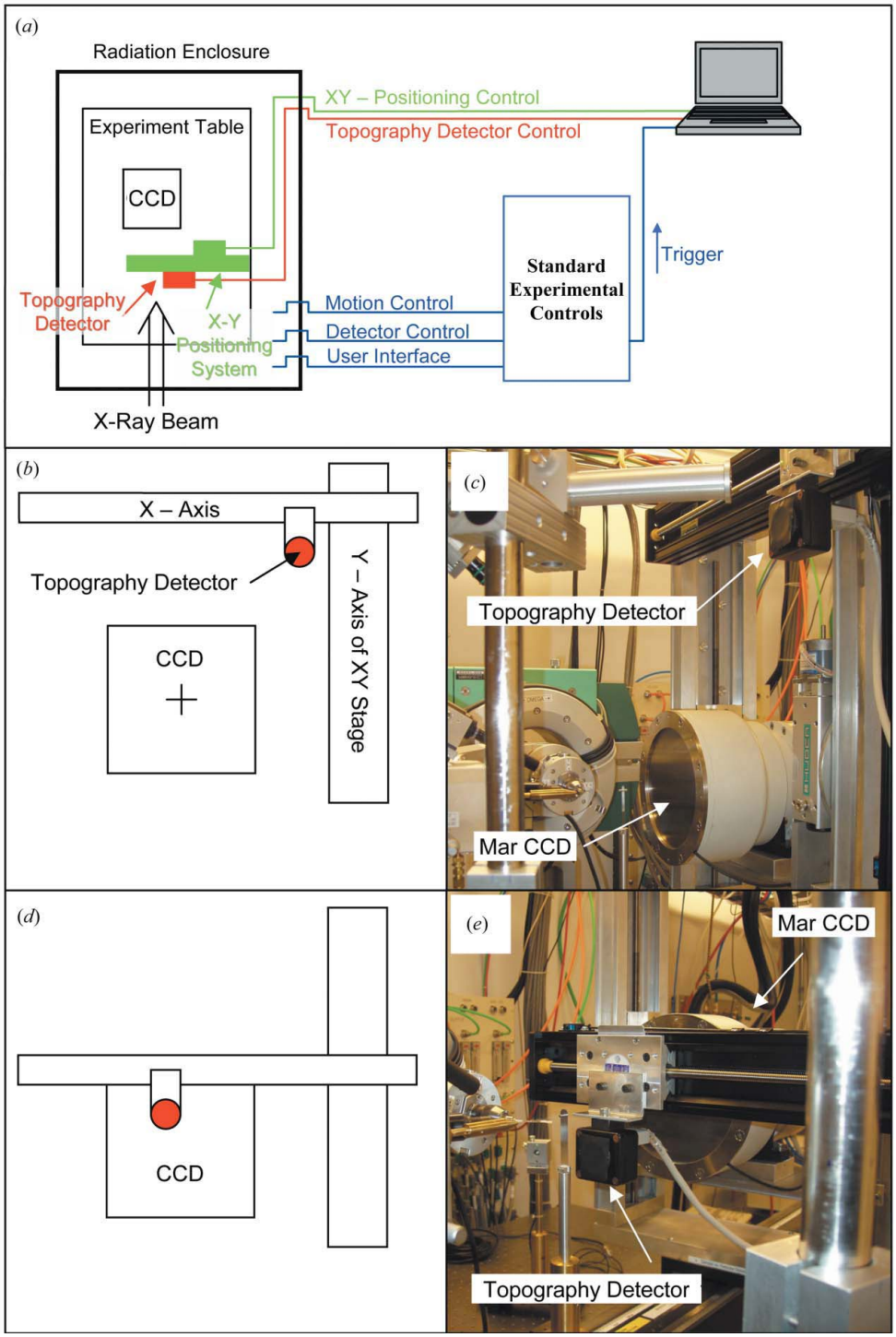

Figure 1
Topography system operation and layout. (*a*) System control schematic showing the MarCCD detector (black square), *X*–*Y* stage (solid green), the topography detector (small solid red rectangle), the shutter control (blue) and the laptop controlling the topography-related components. (*b*) Schematic drawing of detector positions when the MarCCD detector is in use and topography detector (solid red circle) is moved aside. (*c*) Actual image of the experimental setup with the topography detector in the parked position. (*d*) Schematic drawing of detector positions when the topography detector is positioned for use in front of the MarCCD. (*e*) Actual image of the experimental setup with the topography detector in use. This figure is in color in the electronic version of this paper..

in a 70:30 ratio, Hampton Research). For RT data collection, tetragonal lysozyme crystals were mounted in capillaries with a slug of mother liquor in the capillary.

2.2. Overall experimental setup

BioCARS beamline 14-BM-D at the Advanced Photon Source (APS) was used in unfocused mode to minimize beam divergence (Bellamy *et al.*, 2000). The vertical and horizontal beam divergences were determined to be 22 and 45–90 µrad, respectively, and $\Delta\lambda/\lambda$ was 4.00×10^{-4}. Two basic types of diffraction experiments were performed. One was fine φ slicing to measure many reflection profiles using a MarCCD detector (Fig. 1). The other was the collection of single-reflection topographs using a high-resolution imaging CCD. The topography system was installed at the beamline as shown in Fig. 1. The topography detector and motion system were operated by a laptop: UDP (User Datagram Protocol) multicast packets emitted by the BioCARS control software provided exposure control for the topography detector, synchronizing its operation with the beamline hardware (Fig. 1*a*).

This approach has several benefits. The standard beamline control software can be used to collect the topographic data and, since the only connection to the existing hardware is one way (the laptop only listens for the appropriate packets) it is very easy to install and remove the topography equipment with no effect on the existing beamline hardware (Fig. 1*a*). Set-up and tear-down times were ∼30 min each. When not needed, the topography detector was stored out of the way as shown in Figs. 1(*b*) and 1(*c*) so that the regular detector could be positioned at approximately the same crystal-to-detector distance. Two orthogonal translation stages (Velmex BiSlides) allow the topography detector to be positioned exactly where the standard CCD indicated the presence of suitable reflections. The mechanical system in this arrangement provides *X*–*Y* positional control with *Z* being along the X-ray beam. A schematic

drawing and picture of the setup with the topography CCD positioned to capture images is shown in Figs. 1(*d*) and 1(*e*). Capturing topographs and controlling the stage were accomplished using a package developed in-house on a computer running the MS Windows operating system.

The topography system utilizes a TC-281 CCD in the core of the Electrim EDC-2000 detector with an active area of 8 mm × 8 mm and 8 µm × 8 µm pixels. Pixels can be read out in 10 or 8 bit resolution. Detailed specifications for the CCD can be found on the Texas Instruments website (http://www.ti.com).

Table 1
MarCCD data summary.

	Starting coarse φ ($\Delta\varphi$)	Starting fine φ ($\Delta\varphi$)	No. of coarse/fine images	No. of reflections	Mosaicity at FWHM, η†	Exposure time
RT						
Run 1	0° (1.0°)	1.000° (0.001°)	5/250	93	0.012 (7)°	2 s
Run 2	0° (1.0°)	1.000° (0.001°)	5/250	74	0.014 (11)°	2 s
Cryo						
Run 1	0° (1.0°)	2.00° (0.020°)	5/150	401	0.34 (11)°	2 s
Run 2	0° (1.0°)	2.00° (0.020°)	5/150	395	0.33 (9)°	2 s
Run 3	90° (1.0°)	92.00° (0.010°)	5/300	423	0.29 (12)°	2 s

† Standard deviations are given in parentheses.

2.3. Fine φ-sliced data collection for reflection profiling

In order to obtain a statistically significant number of measurements within a reasonable amount of beam time, reflection profiles were collected with a MarCCD-165 detector using the rotation camera geometry as described elsewhere (Bellamy *et al.*, 2000; Borgstahl *et al.*, 2001; Snell *et al.*, 2001). A summary of the data collection is given in Table 1. For all crystals, 5° swaths of coarse data were collected 90° apart ($\Delta\varphi$ = 1.0° with 5.0 s exposure) and processed with *MOSFLM* (Powell, 1999). Next, an angular range was selected from this data that was within one of the coarse images and fine φ-sliced data were collected as oscillations for reflection profiling and mosaicity measurements. Only a small subset of the angular range was selected because the main goal of this experiment was to find target reflections for the topography system and not to perform large-scale mosaicity and crystal quality measurements. For RT data, 250 images of fine φ-sliced data were collected with $\Delta\varphi$ = 0.001° and 2.0 s exposure time. For cryo crystals, 150 or 300 images were collected over 1.0° with $\Delta\varphi$ = 0.020 or 0.010°, respectively, with 2.0 s exposure times. For the cryo crystal, two swaths of fine sliced data were recorded 90.0° apart. Analysis of the coarse data showed that the space group was $P4_32_12$ with cell dimensions of $a = b$ = 78.7, c = 36.9 Å at cryo, and $a = b$ = 79.1, c = 37.9 Å at RT. The wavelength was set to 0.979 Å and the beam was collimated to 0.3 mm diameter for all measurements. Crystals with dimensions smaller than 0.2 mm in any direction were selected so that the X-ray beam would completely envelop the crystal. The crystal to MarCCD detector distance was 130 mm for all measurements. The data were collected in constant-time mode and not corrected for the change in beam intensity with decaying ring current. Since the APS was not operating in top-up mode, in general the ring current decreased from 100 to 80 mA over a 12 h period between injections. The refills were accomplished with the fill-on-fill approach (no down time between fills) and no beam dumps occurred during data collection. Therefore, the change in beam intensity was negligible during any time a given reflection was active.

2.4. Digital topography data collection

The fine φ-sliced data set was analyzed and then a region of reciprocal space selected that would also allow the topography detector to record multiple topographs with one pass. The direct beam was recorded by a short exposure with the beamstop removed but an attenuator in place to minimize the potential for damage to the CCD. The topography detector was positioned with the stage so that the direct beam would hit the middle of the detector (pixel location x = 500, y = 500). Then the X and Y positions of the stage motors were used to record the topography beam center. The crystal-to-detector distance for the topography detector was 121.5 mm. To position the topography detector, simple geometry was applied to determine where the stage should be positioned for the previously selected reflections. The final position was fine-tuned with a few large angle oscillations to more accurately position the topography detector before topographs were recorded. For this study, topographs were recorded as oscillations of 0.010° or 0.020° for cryo and 0.001° for RT data.

2.5. Data processing for fine φ-sliced reflection profiles

The fine φ-sliced data were processed and the reflection profiles were analyzed using *BEAM-ish 2.0* (Lovelace & Borgstahl, 2003; Lovelace *et al.*, 2000). For each swath of data, *BEAM-ish* uses *MOSFLM* for processing of the coarse images and obtaining the unit-cell dimensions and the crystal orientation matrix. *MOSFLM* produces a list of all the theoretically observable reflections and their expected positions. The fine φ-sliced images for that swath are then all integrated at the predicted reflection positions and the background is subtracted to obtain the reflection profiles (intensity *versus* φ) (Bellamy *et al.*, 2000). The resulting profiles were processed to remove 'zingers' (Borgstahl *et al.*, 2001). In order to be accepted for profile analysis, the reflections had to be sufficiently intense (I_{max} > 1000) and had to have a positive mosaicity (η > 0.000°). The later constraint is needed because *BEAM-ish* can assign negative mosaicities in two ways. The first indicates a problem with the peak detection algorithm (normally occurs for a partially recorded reflection) and the second occurs when the correction is larger than the measured width (normally occurs when a reflection is selected for inte-

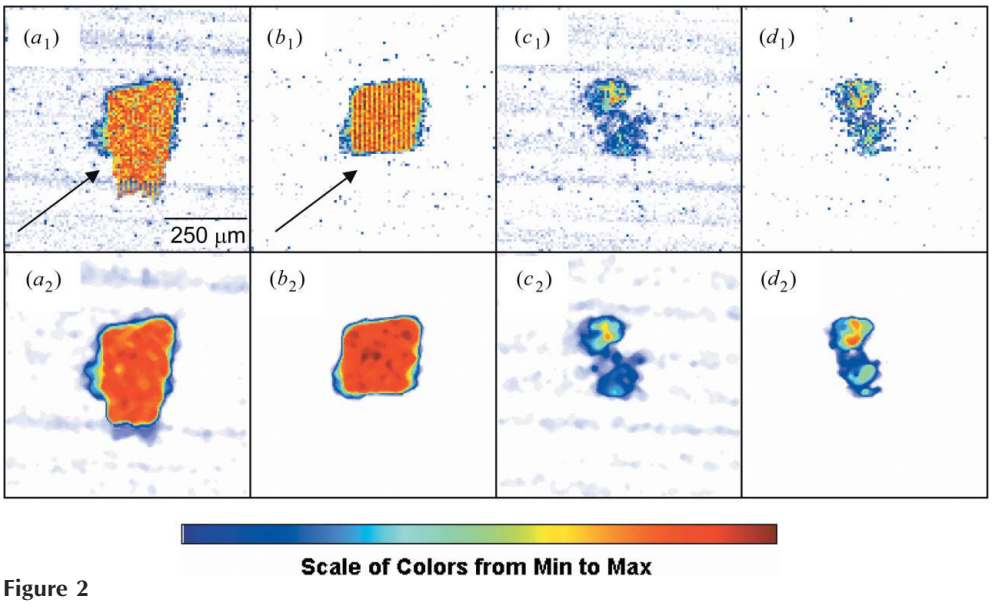

Figure 2
Raw and processed image data shown with the anti-blooming test results from the topography CCD. Raw images are indicated with a subscript number 1. Processed images are indicated with a subscript number 2. (*a*) Image with overloaded pixels and anti-blooming turned off (the arrow indicates the region most greatly affected by blooming). (*b*) Image with overloaded pixels and anti-blooming turned on (the arrow indicates the same region now protected by anti-blooming). (*c*) Image with no overloaded pixels and anti-blooming off. (*d*) Image with no overloaded pixels and anti-blooming on. This figure is in color in the electronic version of this paper.

gration based on indexing but does not actually occur in the image sequence, leaving background noise for the profile). The mosaicity, η, was deconvoluted from the measured reflection full width at half-maximum, φ.

$$\eta = \frac{|\varphi_R| - (L^2\zeta^2\gamma_h^2 + \gamma_v^2)^{1/2}}{Ld^* \cos\theta_{hkl}} - \left(\frac{\delta\lambda}{\lambda}\right)\tan\theta_{hkl}, \qquad (1)$$

where γ_v and γ_h are the vertical and horizontal crossfire angles at the sample, d^* is in r.l.u., $\delta\lambda/\lambda$ is the wavelength range, L is the Lorentz correction, and ζ is the position of the corresponding reciprocal-lattice point projected onto the rotation axis. The effects of these parameters on reflection broadening were described previously (Helliwell, 1992; Bellamy *et al.*, 2000).

2.6. Data processing for digital topography

In the initial step, a reflection topograph was located within the raw data and a 100 × 100 pixel frame was centered over the topograph. Then a stack of frames, each 100 × 100 pixels wide, was extracted from the raw data. After the images were loaded into the stack, a multi-step process was used to clean up and correct the data. The steps included subtraction of the dark current, a genetic-algorithm-based correction of a gain imbalance between odd and even pixels, and wavelet-based resolution enhancement. A detailed example of the processing can be found in the supplementary material.[1] These processing steps vary only slightly from the previous work (Lovelace *et al.*, 2004). In Fig. 2, topographs are shown as raw data (top frames with subscript 1) and after corrections (bottom frames with subscript 2). The processing was carried out using Matlab (The Math Works Inc., 1992).

3. Results

3.1. Test of anti-blooming circuitry

The CCD used in the topography detector incorporates anti-blooming circuitry (Lovelace *et al.*, 2004). Blooming is a problem with CCDs. When a pixel in a CCD accumulates charge beyond the capacity of the pixel well, the excess charge leaks into neighboring pixels. In this case, intensity information that should only occupy a single pixel effectively blooms out to cover many pixels. The idea behind anti-blooming circuitry is to activate a channel between pixels which drains away excess charge that can no longer be held in the pixel. The actual intensity of an overloaded pixel is unknown both with and without the anti-blooming circuitry, but using this feature minimizes intensity errors in neighbouring pixels as well as pixels in the same row as the overloaded pixel. Borders of a reflection should remain crisp with the anti-blooming circuitry enabled.

For this CCD, anti-blooming can be enabled and disabled through the software. A sequence of images was collected with anti-blooming enabled and another with anti-blooming disabled. For an area with several overloaded pixels, the same topography detector location is shown with anti-blooming disabled (Fig. 2*a*) and enabled (Fig. 2*b*). Likewise, for an area with no overloaded pixels, the same location with anti-blooming disabled (Fig. 2*c*) and enabled (Fig. 2*d*) is given. Fig. 2(*a*) shows streaking: as non-overexposed pixels are clocked through the overexposed portion of the CCD chip during the readout process, these pixels pick up some of the excess charge and become overloaded themselves, causing a streak in the image. In Fig. 2(*b*), the anti-blooming circuitry prevents this streaking by limiting both the extent and the magnitude of the excess charge. For the case where no pixels are overloaded there are few differences (Figs. 2*c* and 2*d*), although the background is slightly higher without the anti-blooming circuitry enabled (Fig. 2*c*). Overall, the anti-blooming circuitry improved the topographic images of both high and average intensity reflections.

3.2. Reflection profiles and topographs from RT crystals

Fine φ-sliced RT data were collected for comparison with the cryo data. After processing reflection profiles at the full

[1] Supplementary data are available from the IUCr electronic archives (Reference: HE5319). Services for accessing these data are described at the back of the journal.

width at half-maximum (FWHM), the RT data had an average mosaicity of 0.013° with a standard deviation of 0.007°, based on 167 reflections (Table 1). After reviewing the fine φ-sliced data, a region with observable reflections that had a unique pattern was selected for topographic analysis. A unique pattern was desirable so that the method of positioning the topography detector could be confirmed. This region is shown in Fig. 3(*a*) as a blown-up area of the original MarCCD image that is shown in the background. Fig. 3(*b*) shows the summation of topograph slices through a reflection profile. Two of the reflections were not fully recorded by the topography detector; hence no summation data are available for these (black dashed circles in Figs. 3*a* and 3*b*).

For the RT data, topographs were completely recorded throughout the reflection profile for three reflections. It was more difficult than expected to locate and record the RT reflections for topography. During the experiment, the crystal slipped slightly in the capillary, which altered the crystal orientation and caused the reflection angle φ and the positions x and y to deviate significantly from values recorded with the fine φ-sliced data. Details of the repeatability work are available as part of the supplementary material.

In Fig. 3(*c*), the fine φ-sliced profile for reflection $\overline{18}\,16\,8$ (blue dashed rectangle in Fig. 3*b*) is shown along with topographs from six slices of the reflection. The positions of these slices along the reflection profile are shown with blue vertical lines in Fig. 3(*c*). The reflection appears as two distinct areas simultaneously (first frame); the two regions begin to merge (second frame); the two regions expand into one region (third frame); the reflection begins to recede to the upper left (fourth frame); the reflection continues to recede to the upper left (fifth frame); and finally fades away (sixth frame). This overall pattern was also seen in the other two reflections from this group. The RT reflections also seem to have a crisper border than their cryo counterparts. This shows up as an overall smaller and tighter summation image in total area (Fig. 3*b*) when compared with the cryo results (Fig. 4, next section).

3.3. Reflection profiles and topographs from cryocooled crystals

Two swaths of fine φ-sliced data were collected 90° apart (Fig. 4*b*) on a cryo crystal. Analysis with *BEAM-ish* calculated an average FWHM mosaicity of 0.330° with a standard deviation of about 0.110°, based on 1219 reflections (Table 1). Previously workers have reported mosaicities of 0.47° (Sauter *et al.*, 2001) and ∼0.5 to 1.5° (Kriminski *et al.*, 2002) for cryo lysozyme. Yet, even though this is one of the best reported mosaicity values for cryocooled lysozyme, it corresponds to a twentyfold increase in mosaicity when compared with the RT crystal. From the MarCCD images, again an area with observable reflections that had a unique pattern was selected for topographic analysis. The locations of the two data swaths in reciprocal space are shown in Fig. 4(*b*) by using the Miller indices to project vectors perpendicular to the reflecting planes. The blue lines represent the directions of the unit-cell axes. The sphere is provided to help with depth queuing.

Once the topography detector was moved into position, a topographic data collection run was acquired (Table 2). For the first swath the topographs were recorded as 0.020° oscillations for 100 frames of data (Fig. 4*b*, green lines). The coarse data for this range are shown in Fig. 4(*a*) and as in the first run there were six complete topographs with corresponding fine φ-sliced reflection profiles. The summation of all topographic frames is shown in Fig. 4(a_1). The overall behaviour for this group of reflections was much different from the RT group (Fig. 3). A reflection representative of

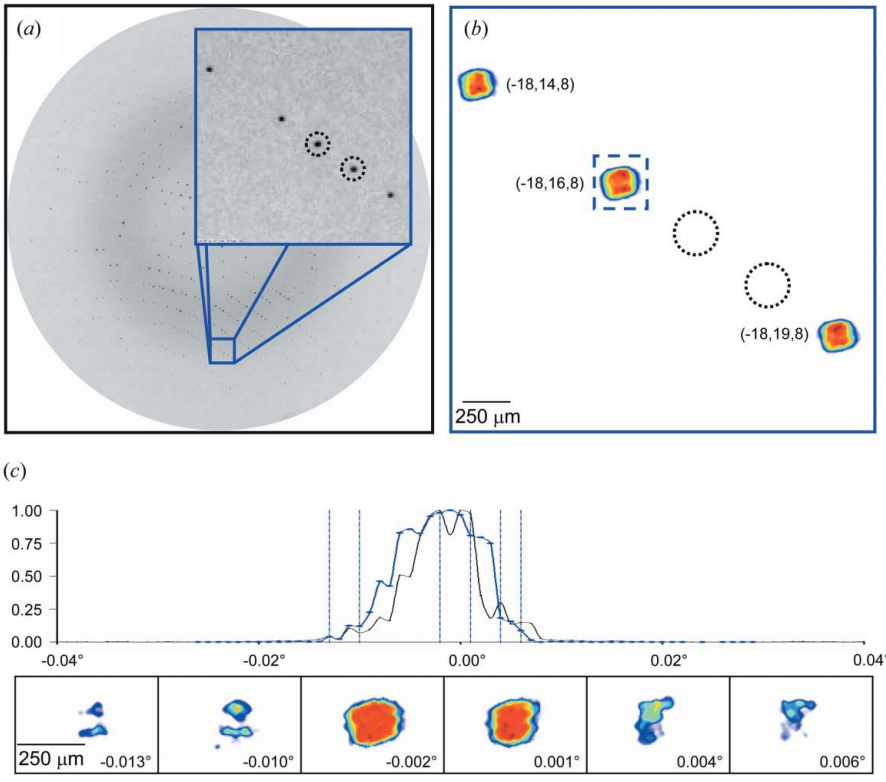

Figure 3
Summary of RT topography data. (*a*) Diffraction image from the MarCCD coarse data with the area used for topography experiments enlarged. (*b*) Summation of topographs of the same reflections in (*a*). Black dashed circles indicate reflections that were only partially recorded during the oscillation. The blue dashed box indicates the reflection used for part (*c*). (*c*) The fine φ-sliced reflection profile (normalized intensity *versus* oscillation angle in degrees) from the MarCCD data (black line) and topography data (blue line) for the $\overline{18}\,16\,8$ reflection. Representative fine sliced topographs are given below the reflection profiles at angles denoted by the vertical blue lines.

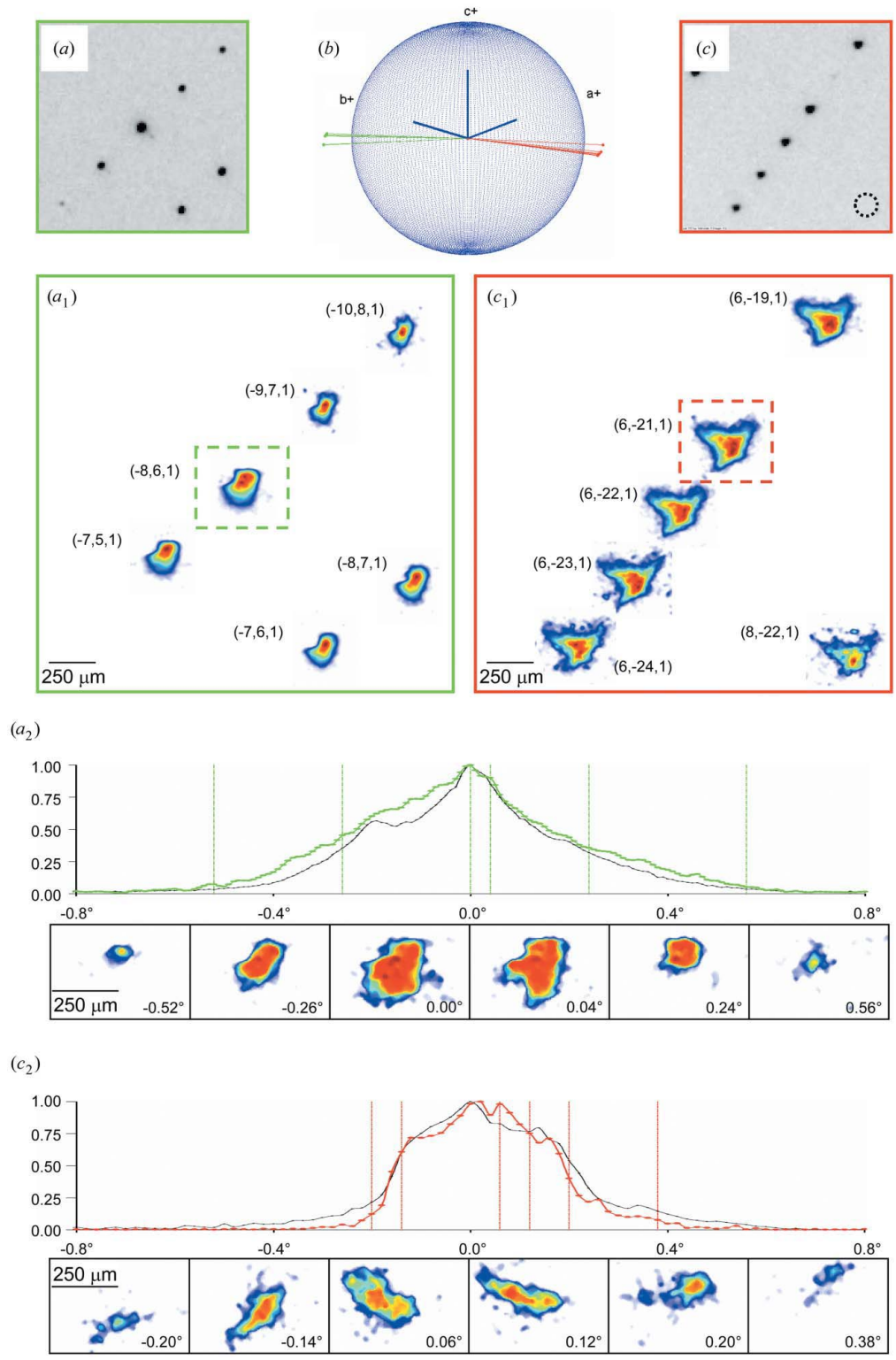

Figure 4
Summary of cryo topography data. (*a*) Enlarged coarse image from the MarCCD where one group of topographs were recorded. (*b*) Schematic visualization of the Miller indices for cryo topograph reflections. (*c*) Enlarged coarse image from the MarCCD where a second group of topographs were recorded. The black dashed circle indicates where no reflection was recorded on the coarse image but was recorded with the topography detector. (a_1) Summation topographs for reflections in part (*a*). The green dashed box indicates the reflection used in part (a_2) below. (c_1) Summation topographs for reflections in part (*c*) above. The red dashed box indicates the reflection used in part (c_2) below. (a_2) The fine φ-sliced reflection profile (normalized intensity *versus* oscillation angle in degrees) from the MarCCD data (black line) and topography data (green line) for the $\overline{8}\,6\,1$ reflection indicated in part (a_1) above. (c_2) The fine φ-sliced reflection profile from the MarCCD data (black line) and topography data (red line) for the $6\,\overline{21}\,1$ reflection indicated in part (c_1) above. In parts (a_2) and (c_2), representative fine sliced topographs are given below the reflection profiles at angles denoted by vertical green and red lines, respectively.

Table 2
Topography CCD data summary.

	Starting φ ($\Delta\varphi$)	No. of frames	Exposure time
RT			
Run 1	1.000° (0.001°)	275	5 s
Cryo			
Run 1	2.00° (0.020°)	100	2 s
Run 3	2.00° (0.020°)	100	2 s

this group, reflection $\overline{8}\,6\,1$ (green dashed rectangle, Fig. 4a_1), is shown with its integrated intensity *versus* φ for both the topographic data and the fine φ-sliced data in Fig. 4(a_2). The two profiles are shown with their intensity normalized and the φ positions shifted such that their peaks are aligned. Six topographs from reflection $\overline{8}\,6\,1$ have been selected to illustrate the entire sequence through the profile. The reflection appears first in the upper half (first frame), expanding down and to the left (second frame), continuing to expand (third frame), indicating some intensity loss in the lower left area (fourth frame), receding up and to the right (fifth and sixth frame). The overall pattern was consistent with the other reflections in this group. A video of this reflection is available as supplementary material.

Another swath of data was collected 90° away (Fig. 4*b*, red lines). The coarse image of the reflections is shown in Fig. 4(*c*). From this scan, six full reflection topographic sequences were recorded on the CCD at one time and a summation of all data frames in the topographic sequence is shown (Fig. 4c_1). All of the reflections have a similar 'butterfly' shape with the most strongly diffracting area located in the lower right of the reflection. Interestingly, one of the reflections that had a good profile and topograph recorded was not visible on the coarse image (the dashed black circle in Fig. 4*c*). This reflection was actually recorded on the previous coarse frame and was therefore near the end of that oscillation in terms of the φ angle. Overall, the six images have slight variations most likely caused by small differences in the angular orientation of the crystal. A reflection representative of the group, reflection $6\,\overline{21}\,1$ (red dashed rectangle in Fig. 4c_1), is shown with its integrated intensity *versus* φ for both the topographic data and the fine φ-sliced data in Fig. 4(c_2). The two profiles are shown normalized to their intensity and their φ positions have been shifted so that the peaks line up with each other. Six topographs from reflection $6\,\overline{21}\,1$ have been selected to illustrate the entire sequence through the profile. As the sequence proceeds, the reflection shifts from lower left (first frame) to the middle (second frame), to the upper left (third frame), to the middle (fourth frame), to the upper right (fifth frame), and finally receded out in the far upper right (sixth frame). All of the frames have been combined into a video, which is available as supplementary material. The overall features described in this example were also observed for the other reflections in this group (Fig. 4c_1).

Other observations relevant for comparison of the two groups of topographs are as follows. The summed reflection topographs are shown inflated to the scale used in the coarse images to highlight better the detail seen in the topographs; yet all topographs (Figs. 3*b*, 4a_1 and 4c_1) are displayed on the same scale. So it can be noted that the RT topographs are smaller (Fig. 3*b*) when compared with the cryo results. It is also noteworthy that the reflections in Fig. 4(c_1) occupy a larger area on the detector than the reflections in Fig. 4(a_1). On the contrary, the group in Fig. 4(c_1) has smaller angular width (Fig. 4c_2) as compared with the other group (Fig. 4a_2).

4. Conclusions

In order to assess the effects of domain misalignment and unit-cell variation on crystal quality, there is a need to measure rapidly reflection topographs and reflection profiles simultaneously. In this study, digital topography has been successfully employed to image directly the mosaic domains of RT and cryo lysozyme crystals, correlated with reflection profiles. Components of the reflections can be identified in the digital topographs, indicating that individual domains have been observed. By making quantitative measurements at different Bragg resolutions in future studies, it should be possible to identify whether these domains are misaligned or have different cell dimensions.

Previous work with film showed spongy topographs for cryo lysozyme crystals as compared with nice crisp boundaries for RT conditions (Kriminski *et al.*, 2002). The digital topographs presented here show similar results. Overall, the rocking profiles, mosaicity and topographs for cryo lysozyme in this study indicate a better crystal quality than reported previously (Kriminski *et al.*, 2002; Sauter *et al.*, 2001). The combination of two cryoprotectants (glycerol and oil) could be responsible for the improved crystal quality. Even with excellent cryoprotection, the well ordered internal mosaic structure of the RT crystals was shattered by cryocooling and caused a dramatic increase in mosaicity.

The novel topography system proved easy to install and operate. Acquisition and processing of topographs were relatively rapid and easy to do when compared with film and nuclear emulsion methods. The anti-blooming circuitry was able to inhibit the effects of overexposed pixels and the detector-acquired data were consistent with traditional film methods. A comparison between these digital topographs and film are available as supplementary material. Difficulties in data collection and interpretation included crystal slippage for RT samples and the use of different crystalline samples for RT and cryo studies. To reduce mechanical effects, stills should be used for fine φ slicing and digital topography. Future work will include reflection profiling and topography at RT and then at cryo temperatures, on the same crystal sample and in identical regions of the reciprocal space. A large range of Bragg resolutions will be studied. Such a well controlled study will provide a better understanding of how mosaic domains are disrupted by cryocooling. The physical basis of annealing and other methods commonly used to improve diffraction will be part of these studies.

NASA Grant NAG8-1983 supported this work. BioCARS receives support (grant RR07707) from the National Center for Research Resources of the National Institutes of Health. We would like to thank the staff at BioCARS for their flexibility and never-ending patience. The pictures from the beamline were provided courtesy of Jay VonOsinski.

References

Bellamy, H. D., Snell, E. H., Lovelace, J., Pokross, M. & Borgstahl, G. E. O. (2000). *Acta Cryst.* D**56**, 986–995.
Boggon, T. J., Helliwell, J. R., Judge, R. A., Olczak, A., Siddons, D. P., Snell, E. H. & Stojanoff, V. (2000). *Acta Cryst.* D**56**, 868–880.
Borgstahl, G. E. O., Vahedi-Faridi, A., Lovelace, J., Bellamy, H. D. & Snell, E. H. (2001). *Acta Cryst.* D**57**, 1204–1207.
Darwin, C. G. (1922). *Philos. Mag.* **43**, 800–829.
Dobrianov, I., Finkelstein, K. D., Lemay, L. G. & Thorne, R. E. (1998). *Acta Cryst.* D**54**, 922–937.
Fourme, R., Ducruix, A., Ries-Kautt, M. & Capelle, B. (1995). *J. Synchrotron Rad.* **2**, 136–142.
Helliwell, J. R. (1988). *J. Cryst. Growth*, **90**, 259–272.
Helliwell, J. R. (1992). *Macromolecular Crystallography with Synchrotron Radiation*. Cambridge University Press.
Kriminski, S., Caylor, C. L., Nonato, M. C., Finkelstein, K. D. & Thorne, R. E. (2002). *Acta Cryst.* D**58**, 459–471.
Lovelace, J. & Borgstahl, G. E. O. (2003). *J. Appl. Cryst.* **36**, 1101–1102.
Lovelace, J., Snell, E. H., Pokross, M., Arvai, A. S., Nielsen, C., Xuong, N.-H., Bellamy, H. D. & Borgstahl, G. E. O. (2000). *J. Appl. Cryst.* **33**, 1187–1188.
Lovelace, J. J., Soares, A. S., Bellamy, H. D., Sweet, R. M., Snell, E. H. & Borgstahl, G. E. O. (2004). *J. Appl. Cryst.* **37**, 481–485.
Lübbert, D., Meents, A. & Weckert, E. (2004). *Acta Cryst.* D**60**, 987–998.
Ludwig, W., Cloetens, P., Hartwig, J., Baruchel, J., Hamelin, B. & Bastie, P. (2001). *J. Appl. Cryst.* **34**, 602–607.
Nave, C. (1998). *Acta Cryst.* D**54**, 848–843.
Otálora, F., García-Ruiz, J. M., Gavira, J. A. & Capelle, B. (1999). *J. Cryst. Growth*, **196**, 546–558.
Powell, H. R. (1999). *Acta Cryst.* D**55**, 1690–1695.
Sauter, C., Otalora, F., Gavira, J.-A., Vidal, O., Giege, R. & Garcia-Ruiz, J. M. (2001). *Acta Cryst.* D**57**, 1119–1126.
Snell, E. H., Judge, R. A., Crawford, L., Forsythe, E. L., Pusey, M. L., Sportiello, M., Todd, P., Bellamy, H., Lovelace, J., Cassanto, J. M. & Borgstahl, G. E. O. (2001). *Cryst. Growth Des.* **1**, 151–158.
Stojanoff, V. & Siddons, D. P. (1996). *Acta Cryst.* A**52**, 498–499.
Stojanoff, V., Siddons, D. P., Monaco, L. A., Vekilov, P. & Rosenberger, F. (1997). *Acta Cryst.* D**53**, 588–595.
Stojanoff, V., Siddons, D. P., Snell, E. H. & Helliwell, J. R. (1996). *Synchrotron Rad. News*, **9**, 25–26.
The Math Works Inc. (1992). *MATLAB Reference Guide*, Natick, MA.
Vahedi-Faridi, A., Lovelace, J., Bellamy, H. D., Snell, E. H. & Borgstahl, G. E. O. (2003). *Acta Cryst.* D**59**, 2169–2182.